A Continuous Fault Ride-through Scheme for DFIGs Under Commutation Failures in LCC-HVDC Transmission Systems

Zixuan Zheng, Donghui Song, Kaijian Du, Xianyong Xiao, Jie Ren, and Qi Xie

***Abstract*—Experimental and theoretical studies have confirmed that, relative to a one-shot voltage fault, a doubly-fed induction generator (DFIG) will suffer a greater transient impact during continuous voltage faults. This paper presents the design and application of an effective scheme for DFIGs when a commutation failure (CF) occurs in a line-commutated converter based high-voltage direct current (LCC-HVDC) transmission system. First, transient demagnetization control without filters is proposed to offset the electromotive force (EMF) induced by the natural flux and other low-frequency flux components. Then, a rotor-side integrated impedance circuit is designed to limit the rotor overcurrent to ensure that the rotor-side converter (RSC) is controllable. Furthermore, coordinated control of the demagnetization and segmented reactive currents is implemented in the RSC. Comparative studies have shown that the proposed scheme can limit rotor fault currents and effectively improve the continuous fault ride-through capability of DFIGs.**

***Index Terms*—Continuous fault, commutation failure (CF), doubly-fed induction generator (DFIG), fault ride-through (FRT) capability, high-voltage direct current (HVDC).**

I. Introduction

To achieve CO_2 emissions peaking before 2030 and carbon neutrality by 2060 in China, large-scale power generation by renewable energy sources transported by line-commutated converter based high-voltage direct current (LCC-HVDC) transmission systems will be more prominent [1]. However, when a commutation failure (CF) occurs on the inverter side of an HVDC system, the fluctuation in the direct current (DC) will cause unbalanced reactive power exchange between the sending alternating current (AC) system and the HVDC system. Thus, it will result in a transient voltage disturbance (TVD) at sending terminals integrated with a high penetration of wind power, which features the "first dip and then rise" process and continuous changes [2]. The point of common coupling (PCC) of wind farms will suffer such transient voltage variations. References [3] and [4] present TVD waveforms recorded in the field. Doubly-fed induction generators (DFIGs), a type of mainstream wind turbine, are sensitive to voltage disturbances because their stators are directly connected to the grid [5]. Compared with a single low-voltage fault, a DFIG will suffer more serious transient impacts and face a greater risk of disconnection from the grid when this new type of fault occurs [6], [7].

Various improved control strategies have been proposed to prevent and mitigate CFs such as optimal control based on the voltage-dependent current order limit (VDCOL) [8] and adaptive extinction angle reference control [9]. Another method is to introduce additional equipment. For example, capacitor-commutated converters can accelerate the commutation process [10]. However, the harmonics and overvoltage issues due to the capacitors should be solved by auxiliary equipment. In practice, more widely applied solutions include the addition of dynamic var sources combined with synchronous condensers [11]-[13].

In order to maintain the stability of the sending terminal during a CF, a DFIG needs to maintain uninterrupted operation. Regarding low-voltage ride through (LVRT) and high-voltage ride through (HVRT), there has been plenty of research that can help a DFIG ride through faults. When a slight low-voltage fault occurs, a reduction in the fault current of the rotor and accelerated attenuation of the natural flux can be achieved by modifying the control strategies of the rotor-side converter (RSC) and grid-side converter (GSC), e.g., demagnetization control [14], double loop control [15], voltage feed-forward control [16], and coordinated current control [17]. However, improved control is only suitable for moderate faults owing to the limited capacities of DFIG converters. Hardware protection is often used to help a DFIG ride through serious faults. The combination of crowbar and chopper circuits is a widely used protection strategy. However, a DFIG becomes an asynchronous motor during the operation of a crowbar and absorbs the reactive power from the grid, which deteriorates the grid voltage [18]. In [19], a static synchronous compensator (STATCOM) is used to output reactive power to increase the terminal voltage during a fault. References [20] and [21] propose a bridge-type fault current limiter (FCL) and a nonlinear current limiter to limit the fault current and increase the termi-

Manuscript received: July 1, 2021; revised: November 8, 2021; accepted: May 28, 2022. Date of CrossCheck: May 28, 2022. Date of online publication: June 27, 2022.

This work was supported by the National Natural Science Foundation of China (No. 51907134).

Z. Zheng, D. Song, K. Du, X. Xiao (corresponding author), J. Ren, and Q. Xie are with the College of Electrical Engineering, Sichuan University, Chengdu, China (e-mail: scuzzx@163.com; 1027684632@qq.com; scudkj@163.com; xiaoxianyong@163.com; renjieholmesjay@163.com; xieqi365@outlook.com).

DOI: 10.35833/MPCE.2021.000441

nal voltage of the stator of a wind turbine, respectively. A dynamic voltage restorer (DVR) is introduced to maintain the terminal voltage of a DFIG in [22], but the DVR requires a large-capacity energy storage device, a high-power converter, and a series transformer with a higher voltage rating for full voltage compensation, resulting in an uneconomical solution. Recently, superconducting-based equipment such as the superconducting fault current limiter (SFCL), superconducting magnetic energy storage (SMES), and SMES-FCL has been designed to realize good fault ride through (FRT) performance [23]-[25]. Although the cost of superconducting tape is decreasing year by year, it remains comparatively high [23].

Owing to DC blocking, a high-voltage fault will occur at the PCC of a wind farm. Although research on HVRT is not as sufficient as that on LVRT, many scholars have also conducted research on it. The virtual damping control is proposed in [26], which can accelerate the attenuation of the natural flux. The influence of the fault duration on the stator flux of a DFIG is analyzed in [27], which adds a compensation term for the stator current to vector control (VC) to limit the rotor current. The deloading operation of a DFIG during the transient period is considered, and the limit of the reactive power output is expanded to reduce the transient overvoltage caused by the DC bipolar block of the HVDC system [28]. An HVRT control method based on resonant controllers is proposed to achieve a smoother transient process in [29]. In [30], control based on a variable reference value for the DC-link voltage is proposed to increase the controllability of a DFIG during faults. In [31], the GSC is in series with the stator to compensate the stator voltage, which can achieve a good transient response. However, a large-capacity converter is required for severe faults. A novel DVR is designed to enhance the HVRT capability of DFIGs in [32], but the designed DVR has a complex structure.

However, LVRT and HVRT are basically studied separately. Few studies have considered continuous faults. The transient characteristics of a DFIG when a step-type continuous fault occurs are analyzed in [33]. The stator current differential is fed-forward to the rotor voltage, which reduces the induced potential and overcurrent of the rotor and enhances the ride-through performance when a continuous fault occurs. In [7], there are low-frequency flux components for the non-speed frequency in the rotor circuit for continuous voltage faults with nonstep changes in amplitude. Thus, a new transient flux observer and an improved control strategy are proposed, which accelerate the attenuation of the transient flux and meet the reactive power requirements of grid connection standards. However, a DFIG cannot ride through serious faults with this improved control owing to the limitation of the rated capacity of the RSC.

This paper presents a new continuous FRT scheme for DFIGs that combines improved control with a current-limiting circuit. The DFIG model under continuous faults is presented in Section II. The proposed continuous FRT scheme is explained in Section III. Simulation studies are conducted to demonstrate the effectiveness of the scheme in Section IV. Finally, conclusions are drawn in Section V.

II. DFIG Model Under Continuous Faults

A. Continuous Fault Mechanism

The configuration of an LCC-HVDC transmission system that includes a wind farm at the sending terminal is shown in Fig. 1. CFs are one of the most common incorrect operations of LCC-HVDC transmission systems. They are often caused by AC system faults at the inverter terminal. When a CF occurs in the inverter station, a decrease in the DC voltage will simultaneously cause the DC current to increase. In order to reduce the DC current, a VDCOL is activated, and constant current control of the rectifier station causes its firing angle to increase rapidly. The reactive power consumed by the rectifier station increases as the firing angle of the rectifier station and the DC current increase. If the reactive power provided by the var compensation devices such as AC filters in the rectifier station is insufficient, the rectifier station will absorb reactive power from the sending AC system, resulting in a decrease in the voltage at the PCC of the wind farm. Until the control strategy of the converter stations reduces the DC current, the reactive power consumed by the rectifier station decreases. However, the reactive power output by the var compensation devices with mechanical switches cannot be adjusted in time with the change in the system operating conditions, and the rectifier station will have surplus reactive power. Thus, a large amount of reactive power is injected into the AC system, which will cause the PCC voltage of the wind farm to increase. If the fault that causes CF is not cleared in time or the LCC-HVDC system is not controlled properly [34], [35], the HVDC system is prone to subsequent CFs. Until the HVDC returns to normal operation, the PCC voltage of the wind farm returns to the normal value.

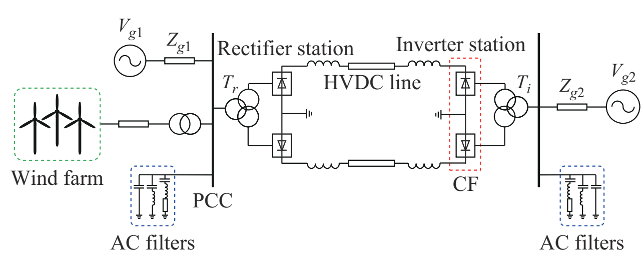

Fig. 1. Configuration of LCC-HVDC transmission system.

B. DFIG Model Under Continuous Faults

Different continuous faults are shown in Fig. 2(a) and (b), which both include a stage where the stator voltage decreases to a low voltage, a stage where the low voltage is sustained, a stage where the stator voltage increases to a high voltage, a stage where the high voltage is sustained, and a recovery stage. k_1, k_2, and k_3 are the rates of change in the voltage amplitude during t_0-t_1, t_2-t_3, and t_4-t_5, respectively. In Fig. 2(a), the root mean square (RMS) error of stator voltage $U_{R\text{-}MS}$ decreases to $1-P_1$ at a rate of k_1 and is maintained at $1-P_1$ over t_1-t_2. Then, it rises to $1+P_2$ at a rate of k_2, keeps unchanged for a period of time, and finally returns to the rated value at a rate of k_3. A single complete continuous fault in Fig. 2(a) is defined as the process in which the voltage first decreases, then increases to a high value, and finally returns to the rated value. Multiple continuous faults can be defined as multiple "decrease first and then increase" processes, as shown in Fig. 2(b).

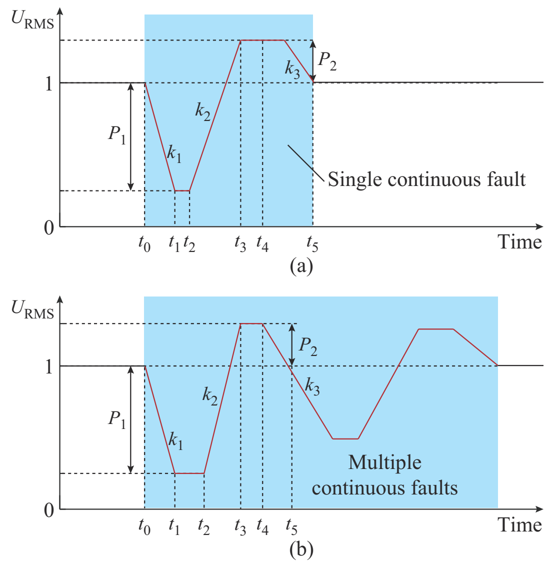

Fig. 2. RMS of stator voltage of DFIG under single continuous fault or multiple continuous faults. (a) Single continuous fault. (b) Multiple continuous faults.

The DFIG voltage and flux equations in the stationary stator reference frame can be expressed as:

$$\begin{cases} \boldsymbol{v}_s^s = R_s \boldsymbol{i}_s^s + \dfrac{\mathrm{d}}{\mathrm{d}t}\boldsymbol{\psi}_s^s \\ \boldsymbol{v}_r^s = R_r \boldsymbol{i}_r^s + \dfrac{\mathrm{d}}{\mathrm{d}t}\boldsymbol{\psi}_r^s - \mathrm{j}\omega_r \boldsymbol{\psi}_r^s \end{cases} \tag{1}$$

$$\begin{cases} \boldsymbol{\psi}_s^s = L_s \boldsymbol{i}_s^s + L_m \boldsymbol{i}_r^s \\ \boldsymbol{\psi}_r^s = L_r \boldsymbol{i}_r^s + L_m \boldsymbol{i}_s^s \end{cases} \tag{2}$$

where $\boldsymbol{v}$, $\boldsymbol{i}$, and $\boldsymbol{\psi}$ are the voltage, current, and flux space vectors, respectively; the subscripts s and r denote the stator and the rotor, respectively; the superscript s denotes the stationary stator reference frame; R_s and R_r are the stator and rotor resistances, respectively; L_s, L_r, and L_m are the stator, rotor, and magnetizing inductances, respectively; and ω_r is the angular frequency of the rotor.

It can be observed that, unlike a step-type low-voltage fault, the voltage amplitude of a continuous fault does not suddenly change but first decreases and then transitions to a high value after some time. According to [7], when the voltage amplitude linearly decreases, the stator flux can be calculated as:

$$\boldsymbol{\psi}_s^s = \frac{[1-k_1(t-t_0)]\boldsymbol{v}_s^s}{\mathrm{j}\omega_s} - \frac{k_1 \boldsymbol{v}_s^s}{\omega_s^2} + C_1 \mathrm{e}^{-\frac{t-t_0}{\tau}} \quad t_0 \le t \le t_1 \tag{3}$$

where $\tau = L_s/R_s$ is the decay time constant of the natural flux of the stator; ω_s is the angular frequency of the stator; and C_1 is the initial value of the natural flux.

According to the flux continuity theorem, the stator flux during the entire fault period can be obtained as:

$$\boldsymbol{\psi}_s^s = \begin{cases} \dfrac{[1-k_1(t-t_0)]\boldsymbol{v}_s^s}{\mathrm{j}\omega_s} - \dfrac{k_1 \boldsymbol{v}_s^s}{\omega_s^2} + C_1 \mathrm{e}^{-\frac{t-t_0}{\tau}} & t_0 \le t \le t_1 \\ \dfrac{(1-P_1)\boldsymbol{v}_s^s}{\mathrm{j}\omega_s} + C_2 \mathrm{e}^{-\frac{t-t_1}{\tau}} & t_1 \le t \le t_2 \\ \dfrac{[1+k_2(t-t_0)]\boldsymbol{v}_s^s}{\mathrm{j}\omega_s} + \dfrac{k_2 \boldsymbol{v}_s^s}{\omega_s^2} + C_3 \mathrm{e}^{-\frac{t-t_2}{\tau}} & t_2 \le t \le t_3 \\ \dfrac{(1+P_2)\boldsymbol{v}_s^s}{\mathrm{j}\omega_s} + C_4 \mathrm{e}^{-\frac{t-t_3}{\tau}} & t_3 \le t \le t_4 \end{cases} \tag{4}$$

where C_2, C_3, and C_4 are the initial values of the natural flux during different stages.

In (4), C_1, C_2, C_3, and C_4 can be expressed as:

$$\begin{cases} C_1 = \dfrac{k_1 v_s^s \mathrm{e}^{\mathrm{j}\omega_s t_0}}{\omega_s^2} & t_0 \le t \le t_1 \\ C_2 = -\dfrac{k_1 v_s^s}{\omega_s^2}\mathrm{e}^{\mathrm{j}\omega_s t_1} + C_1 \mathrm{e}^{-\frac{t_1-t_0}{t}} & t_1 \le t \le t_2 \\ C_3 = -\dfrac{k_2 v_s^s}{\omega_s^2}\mathrm{e}^{\mathrm{j}\omega_s t_2} + C_2 \mathrm{e}^{-\frac{t_2-t_1}{t}} & t_2 \le t \le t_3 \\ C_4 = \dfrac{k_2 v_s^s}{\omega_s^2}\mathrm{e}^{\mathrm{j}\omega_s t_3} + C_2 \mathrm{e}^{-\frac{t_3-t_2}{t}} & t_3 \le t \le t_4 \end{cases} \tag{5}$$

where v_s^s is the voltage magnitude.

According to (1) and (2), the rotor voltage can be obtained as:

$$\boldsymbol{v}_r^s = \frac{L_m}{L_s}\left(\frac{\mathrm{d}}{\mathrm{d}t}\boldsymbol{\psi}_s^s - \mathrm{j}\omega_r \boldsymbol{\psi}_s^s\right) + R_r \boldsymbol{i}_r^s + \sigma L_r\left(\frac{\mathrm{d}}{\mathrm{d}t}\boldsymbol{i}_r^s - \mathrm{j}\omega_r \boldsymbol{i}_r^s\right) \tag{6}$$

The first item on the right-hand side of (6) is the open-circuit voltage of the rotor, i.e., the rotor-induced electromotive force (EMF). The rotor EMF during t_3-t_4 can be calculated as:

$$\begin{aligned} \boldsymbol{e}_r^s = {} & \frac{L_m}{L_s}s(1+P_2)v_s^s \mathrm{e}^{\mathrm{j}\omega_s t} - \frac{L_m}{L_s}(1-s)\Bigg(k_2 \frac{v_s^s}{\omega_s}\mathrm{e}^{\mathrm{j}\omega_s t_3}\mathrm{e}^{-\frac{t-t_3}{\tau}} - \\ & k_2 \frac{v_s^s}{\omega_s}\mathrm{e}^{\mathrm{j}\omega_s t_2}\mathrm{e}^{-\frac{t-t_2}{\tau}} - k_1 \frac{v_s^s}{\omega_s}\mathrm{e}^{\mathrm{j}\omega_s t_1}\mathrm{e}^{-\frac{t-t_1}{\tau}} + k_1 \frac{v_s^s}{\omega_s}\mathrm{e}^{\mathrm{j}\omega_s t_0}\mathrm{e}^{-\frac{t-t_0}{\tau}}\Bigg) = \\ & \frac{L_m}{L_s}s(1+P_2)v_s^s \mathrm{e}^{\mathrm{j}\omega_s t} - \frac{L_m}{L_s}(1-s)\Bigg(\frac{P_1+P_2}{t_3-t_2}\frac{v_s^s}{\omega_s}\mathrm{e}^{\mathrm{j}\omega_s t_3}\mathrm{e}^{-\frac{t-t_3}{\tau}} - \\ & \frac{P_1+P_2}{t_3-t_2}\frac{v_s^s}{\omega_s}\mathrm{e}^{\mathrm{j}\omega_s t_2}\mathrm{e}^{-\frac{t-t_2}{\tau}} - \frac{P_1}{t_1-t_0}\frac{v_s^s}{\omega_s}\mathrm{e}^{\mathrm{j}\omega_s t_1}\mathrm{e}^{-\frac{t-t_1}{\tau}} + \\ & \frac{P_1}{t_1-t_0}\frac{v_s^s}{\omega_s}\mathrm{e}^{\mathrm{j}\omega_s t_0}\mathrm{e}^{-\frac{t-t_0}{\tau}}\Bigg) \end{aligned} \tag{7}$$

If only one high-voltage fault with a step increase has occurred after the steady-state operation, the open-circuit voltage of the rotor is:

$$\boldsymbol{e}_{r,step}^s = \frac{L_m}{L_s}s(1+P_2)v_s^s \mathrm{e}^{\mathrm{j}\omega_s t} - \frac{L_m}{L_s}(1-s)P_2 v_s^s \mathrm{e}^{-\frac{t}{\tau}} \tag{8}$$

It can be observed from (7) and (8) that the voltage swell of a continuous fault is different from a single voltage swell, which is affected by the low-voltage stage of a continuous fault. The EMF induced in the high-voltage stage is greater when the decrease in the voltage is higher and the time over which the voltage decrease occurs is shorter. Compared with a single fault, the transient flux component generated in the previous stage will be superimposed on the latter stage, resulting in a larger rotor EMF, which causes the RSC to face larger fault currents and threatens the safe operation of wind turbines. Therefore, the effect of the accumulated stator flux should be mitigated while limiting the fault current of the rotor to reduce the harm to the DFIG due to continuous faults.

III. Proposed Continuous FRT Scheme

A. Improved Demagnetization Control

According to [14], a current component can be injected into the rotor that is opposite to the other low-frequency components to counteract the non-power frequency flux component. Reference [7] proposes an improved transient flux observer to extract the transient component of the stator flux during a continuous fault. However, the effect of control is affected by the phase lag of the low-pass filter. An improved demagnetization control without the filter is proposed, and its control block diagram is shown in Fig. 3.

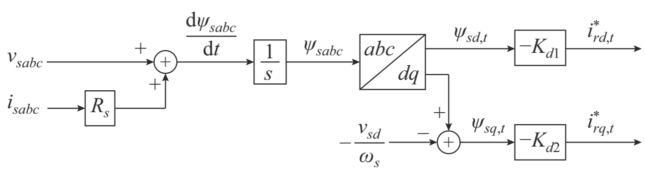

Fig. 3. Block diagram of improved demagnetization control.

As shown in Fig. 3, the control loop adopts d-axis voltage (v_{sd}) oriented control. First, the stator flux differential is calculated from the stator voltage v_{sabc} and stator current i_{sabc}. Then, the three-phase stator flux ψ_{sabc} can be obtained with the integrator. Because of the d-axis voltage oriented control, the forced component of the d-axis flux should be zero. Therefore, the transient component of the d-axis stator flux $\psi_{sd,t}$ can be directly obtained. Regardless of the stator resistance, the transient component of the q-axis stator flux $\psi_{sq,t}$ can be obtained by subtracting the forced component of the q-axis flux from the q-axis stator flux.

The transient demagnetization current in the improved control can be expressed as:

$$\begin{cases} i^*_{rd,t} = -K_{d1}\psi_{sd,t} \\ i^*_{rq,t} = -K_{d2}\psi_{sq,t} \end{cases} \tag{9}$$

where $i^*_{rd,t}$ and $i^*_{rq,t}$ are the d- and q-axis demagnetization currents of the rotor, respectively; and K_{d1} and K_{d2} are the compensation coefficients, which are positive.

A larger compensation coefficient can better restrain the rotor overcurrent, but the RSC output voltage is higher. A smaller compensation coefficient will lower the output voltage of the RSC and weaken the ability to restrain the rotor overcurrent. The introduction of demagnetization current in the active current loop will cause an instantaneous active power and electromagnetic torque pulsation. In this study, two types of compensation coefficients are designed, which can reduce K_{d1} in the case of shallow faults, thereby preventing a large active power and electromagnetic torque pulsation. In the case of deep faults, K_{d1} and K_{d2} can take the same limiting value to accelerate the attenuation of the transient stator flux.

B. Series Impedance of Rotor

Owing to the limited capacity of the RSC, the magnitude of the demagnetization current for deep faults will exceed the allowable current of the RSC. The peak value of the output voltage of the RSC cannot exceed the DC voltage; hence, the output voltage of the RSC should be within a certain range. From (6), it can be observed that it is the difference between the EMF and the rotor voltage that produces a larger current in the transient impedance of the rotor. Therefore, an increase in the impedance of the rotor can limit the fault current of the rotor. It can be observed from [36] that the insertion of a large resistance into the rotor circuit easily leads to a higher rotor voltage. Although the inductance inserted into the rotor can limit the current, it increases the time constant of the rotor and slows down the transient attenuation. However, since the output voltage of the GSC is limited by the modulation ratio, it will cause the DC-link voltage to increase in the high-voltage stage. Thus, a DC chopper is used to protect the DC-link circuit.

A control system for a DFIG integrated with the proposed scheme is shown in Fig. 4, where PLL stands for phase-locked loop and SPWM stands for sinusoidal pulse width modulation; V_{pccN} and V_{pcc} are the rated and actual PCC voltages, respectively; P^*_s and P_s are the reference and actual values of the active power of the stator, respectively; Q^*_s and Q_s are the reference and actual values of the reactive power of the stator, respectively; V^*_{rd} and V^*_{rq} are the reference values of the d- and q-axis voltages of the rotor, respectively; σ is the leakage inductance coefficient; V^*_{dc} and V_{dc} are the reference and actual values of the DC-link voltage, respectively; Q^*_g and Q_g are the reference and actual values of the reactive power on the grid side, respectively; i_{gd} and i_{gq} are the actual values of the d- and q-axis currents of the rotor, respectively; i^*_{gd} and i^*_{gq} are the reference values of the d- and q-axis currents of the rotor, respectively; V^*_{gd} and V^*_{gq} are the reference values of the d- and q-axis GSC output voltage, respectively; i_{rd} and i_{rq} are the actual values of the d- and q-axis currents of the rotor, respectively; i^*_{rd1} and i^*_{rq1} are the reference values of the positive-sequence active and reactive currents of the rotor, respectively; S_a, S_b, and S_c are the three-phase output signals of hysteresis comparators; K'_d is the modified demagnetization coefficient; $\theta = -\arctan(R'_r/(\omega_r L'_{r\sigma}))$, R'_r and $L'_{r\sigma}$ are the equivalent transient resistance and inductance, respectively; ψ_{sd} is the d-axis stator flux; θ_g is the grid voltage phase; $\psi_{s,t}$ is the stator transient flux; R_{sr} and L_{sl} are the series resistance and inductance, respectively; and L_g and R_g are the inductance and resistance of the grid-side filter, respectively. When the PCC voltage is less than $0.9V_{pccN}$ or greater than $1.1V_{pccN}$, a fault is detected. Then, the series impedance of the rotor is activated to limit the fault current of the rotor and accelerate the decay of the stator flux. When the PCC returns to the normal operation range, the series impedance of the rotor is cut off after a time delay.

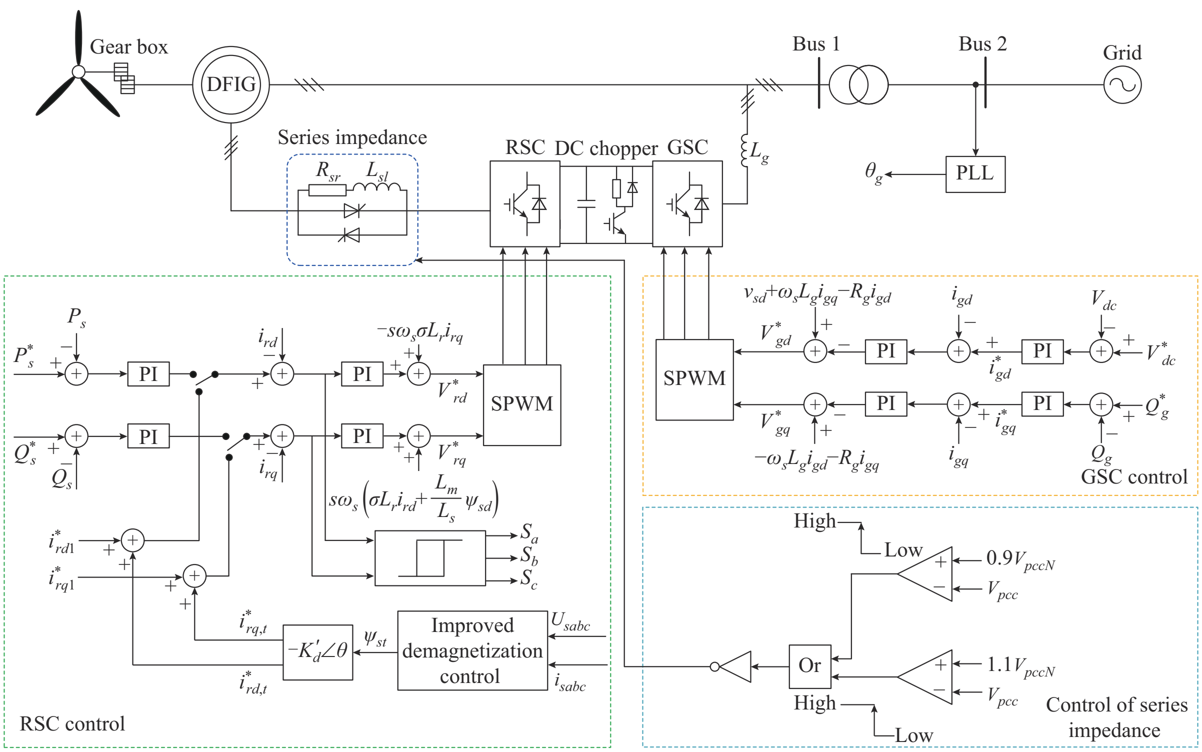

Fig. 4. Control system for a DFIG integrated with proposed scheme.

After inserting the impedance, the rotor voltage can be expressed as:

$$\boldsymbol{v}_r^r=\boldsymbol{e}_r^r+(R_r+R_{sr})\boldsymbol{i}_r^s+(\sigma L_r+L_{sl})\frac{\mathrm{d}}{\mathrm{d}t}\boldsymbol{i}_r^r=\boldsymbol{e}_r^s+R_r'\boldsymbol{i}_r^r+L_r'\frac{\mathrm{d}}{\mathrm{d}t}\boldsymbol{i}_r^r \tag{10}$$

where R_r' and L_r' are the equivalent transient resistance and inductance of the rotor, respectively.

According to (1) and (2), the stator voltage can be re-expressed as:

$$\boldsymbol{v}_s^s=R_s'\boldsymbol{i}_s^s+\sigma L_s\frac{\mathrm{d}\boldsymbol{i}_s^s}{\mathrm{d}t}+\frac{L_m}{L_r'}\left(\boldsymbol{v}_r^s+\mathrm{j}\omega_r\boldsymbol{\psi}_r^s-\frac{R_r'\boldsymbol{\psi}_r^s}{L_r'}\right) \tag{11}$$

where $R_s'=R_s+L_m^2R_r'/L_r'$ is the transient resistance of the stator.

It can be observed from (11) that the attenuation of the transient flux of the stator can be accelerated by selecting a suitable impedance value according to (3).

The selection of impedance parameters should be considered on the basis of more serious conditions. According to (4)-(7), for typical low- and high-voltage continuous faults, the most serious situation is that the transient flux induced by a low-voltage fault and the transient flux induced by a high-voltage fault are in the same direction. In addition, both low- and high-voltage faults can be considered to be step-type faults since the amplitude of the transient flux generated by a step-type voltage fault is greater than that of a voltage fault with a certain change over time. In a relatively short time, two faults can be equivalent to a single voltage fault, ignoring the attenuation of the transient flux. At this time, the series impedance is inserted into the rotor. According to transient analyses of the rotor current in [23], [37], the peak rotor current can be calculated as:

$$\begin{aligned}I_{rp}=\Bigg|&\frac{V_{rm}-k_sv_s(1+P_2)}{R_r'+\mathrm{j}s\omega_sL_{r\sigma}'}\mathrm{e}^{\frac{\mathrm{j}\omega_sT}{2}}-\frac{k_sv_s(2P_1+P_2)(1-s)}{R_r'-\mathrm{j}s\omega_sL_{r\sigma}'}\mathrm{e}^{-\frac{(\mathrm{j}\omega_r+R_s/L_s)T}{2}}+\\&\left[i_r(0_-)-\frac{V_{rm}-k_ssv_s(1+P_2)}{R_r'+\mathrm{j}s\omega_sL_{r\sigma}'}+\frac{k_sv_s(2P_1+P_2)(1-s)}{R_r'-\mathrm{j}s\omega_sL_{r\sigma}'}\right]\mathrm{e}^{-\frac{TR_r'}{2L_{r\sigma}'}}\Bigg|\end{aligned} \tag{12}$$

where V_{rm} is the maximum output voltage of the RSC; $k_s=L_m/L_s$ is the coupling factor of the stator; and $i_r(0_-)$ is the prefault current.

The impedance parameters can be selected according to (12). Although the overcurrent of the rotor can be limited more extensively when the selected impedance parameters are larger, this may weaken the controllability of the RSC and result in overvoltage of the rotor. The resistance and reactance of the series impedance in this paper are 25.2 mΩ and 5.7 mH, respectively.

C. Coordinated Control

1) Segmented Reactive Current Control

Multiple grid codes require a DFIG to support the grid voltage during a fault; that is, the DFIG should absorb/output additional reactive power.

The E.ON grid code requires a wind turbine to have LVRT capability and the ability to provide dynamic reactive and voltage support. Taking the E.ON grid code as an example, the additional reactive current of the stator i_{sq1}^* when a voltage dip and swell fault occurs needs to satisfy:

$$\begin{cases}i_{sq1}^*=2(v_s-1) & 0.5\text{ p.u.}\le v_s<0.9\text{ p.u. or } v_s>1.1\text{ p.u.}\\ i_{sq1}^*\ge 1 & 0\le v_s<0.5\text{ p.u.}\end{cases} \tag{13}$$

According to the relationship between the stator and rotor currents, the q-axis reactive current reference of the rotor can be set as:

$$i_{rq1}^{*}=-\frac{L_s}{L_m}i_{sq1}^{*}-\frac{v_s}{\omega_s L_m} \tag{14}$$

According to (13) and (14), the segmented reactive current strategy proposed in this paper includes two modes, i.e., the reactive current output mode during the low-voltage stage and the reactive current absorption mode during the high-voltage stage. In addition, it can be observed from Fig. 2 that the grid voltage continuously changes in a short time, and the reactive current requires the output to change rapidly. Proportional-integral (PI) controllers have good performance in the steady state. However, the transient response speed of PI controllers is low, which will lead to larger tracking errors [16]. Here, a hysteresis current regulator with a simple structure and strong robustness is selected during a fault.

2) Modified Transient Demagnetization Control

After the current-limiting impedance is activated on the rotor side, the equivalent impedance of the rotor increases. Compared with the situation in which there is no series impedance, the amplitude and phase of the demagnetization current need to be modified. In order to offset the transient component of the EMF caused by the transient flux, the demagnetization current needs to satisfy:

$$\mathrm{j}\omega_r\frac{L_m}{L_s}\boldsymbol{\psi}_{s,t}^{r}+[R_r+R_{sr}+\mathrm{j}\omega_r(\sigma L_r+L_{sl})]\boldsymbol{i}_{r,t}^{r}=0 \tag{15}$$

From (15), the demagnetization current is:

$$\boldsymbol{i}_{r,t}^{r}=-\frac{L_m}{L_s}\frac{\omega_r\boldsymbol{\psi}_{s,t}^{r}}{\sqrt{R_r'+\mathrm{j}\omega_r L_{r\sigma}'}}\angle\theta=-K_d'\boldsymbol{\psi}_{s,t}^{r}\angle\theta \tag{16}$$

According to (15), the demagnetization current is injected into the rotor current reference, which can offset the EMF of the rotor and accelerate the attenuation of the transient flux of the stator. According to (16), the amplitude of the transient demagnetization current greatly decreases owing to the increase in the transient impedance of the rotor.

D. Operation Sequence

A flowchart of the proposed scheme is shown in Fig. 5, which can be described as follows.

1) The series impedance is inserted into the rotor when a fault is detected to limit the fault current of the rotor and ensure that the RSC can be controlled.

2) The active current is set to be 0 to ensure that the RSC has sufficient current capacity for the demagnetization current, the reactive current, and part of the active current. On the basis of the series impedance parameters and the grid voltage level, coordinated control can be implemented according to (14) and (16).

3) When the voltage returns to the normal range, the active and additional reactive currents are reset to be 0 after a delay of 50 ms. After a delay of 100 ms, the series impedance is deactivated to ensure that the DFIG is not affected when the series impedance is cut off. Finally, the DFIG returns to steady-state operation after a delay of 50 ms.

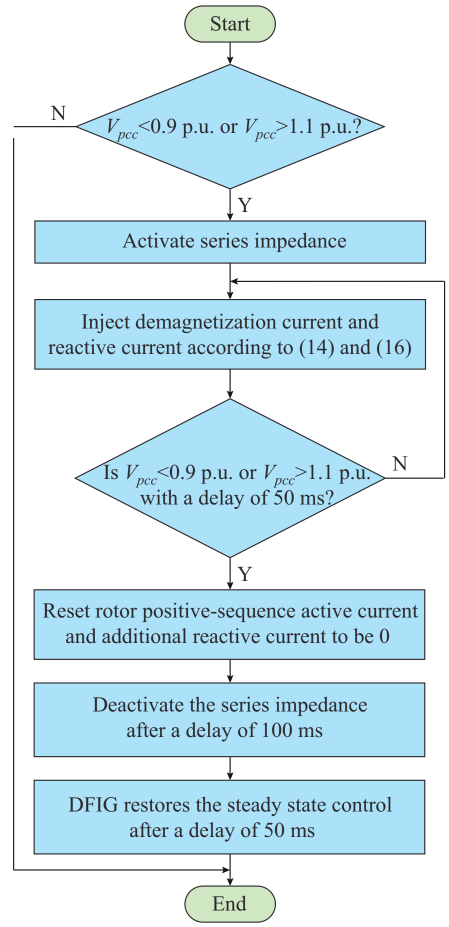

Fig. 5. Flowchart of proposed scheme.

IV. Simulation Results

The 1.5 MW DFIG shown in Fig. 4 is built in MATLAB/ Simulink. It delivers 1.5 MW of active power and 0 Mvar of reactive power to the grid. At the same time, it is assumed that the wind speed during the fault remains unchanged. The AC grid voltage is realized by three controlled voltage sources (CVSs), and the output voltage of the CVSs is driven by the input signal. The parameters of the DFIG in the simulation are listed in Table I.

TABLE I
Parameters of DFIG in Simulation

Parameter	Value
Rated power	1.5 MW
Stator voltage	690 V
Rotor voltage	1725 V
DC-link voltage	1200 V
Stator resistance	0.005 p.u.
Stator inductance	0.171 p.u.
Rotor resistance	0.007 p.u.
Rotor inductance	0.156 p.u.
Mutual inductance	2.9 p.u.
Grid frequency	50 Hz

A. Behaviors with Improved Demagnetization Control

To verify the effectiveness of the proposed improved demagnetization control, the RSC uses different current control strategies. During a fault, the active current reference is set to be 0, and the reactive current reference still retains its pre-fault value. Moreover, the demagnetization current is added to the rotor current. The following four control strategies are considered.

1) Strategy A: the conventional demagnetization control strategy in [14].

2) Strategy B: the improved control strategy in [7], which does not use a band-pass filter to filter the DC component of the stator flux.

3) Strategy C: the natural stator current tracking control strategy in [38], which adopts a low-pass filter to extract the natural component of the stator current.

4) Strategy D: the proposed improved demagnetization control strategy.

Figure 6 shows the simulation results of DFIG with different control strategies under the single continuous fault. As shown in Fig. 6(a), the stator voltage decreases to 0.4 p.u. within 10 ms, then increases to 1.35 p.u. within 10 ms, and maintains a high voltage for a period of time. As shown in Fig. 6(b), the rotor current amplitudes under Strategy A and Strategy D are 2.435 and 2.331 p.u., respectively, showing that Strategy D has a better current-limiting effect. The maximum current amplitude is 3.393 p.u. for Strategy C because it is difficult to accurately track the natural stator current with this control strategy. According to Fig. 6(c), Strategy D and Strategy A have similar limiting effects on the DC-link voltage. It can be observed from Fig. 6(e) that torque oscillation has the smallest peak-to-peak value for Strategy D with an amplitude of 5.27 p.u..

B. Behaviors Under Single Severe Continuous Fault

Although the improved demagnetization control has a certain limiting effect on the fault current, the demanded demagnetization current is very large, and the safe operation of a DFIG cannot be guaranteed when severe faults occur. Comparative studies have been conducted. The following three schemes and the proposed scheme are considered.

1) Scheme A: with conventional VC.

2) Scheme B: with the crowbar and DC-chopper combination.

3) Scheme C: with an energy storage inverter connected in parallel on the rotor side and coordinated control of the demagnetization and reactive currents in [39].

The simulation results under a single continuous fault with different schemes are shown in Fig. 7. The first low-voltage fault of the grid voltage starts at 0.1 s and decreases to 0.2 p.u. within 10 ms. Then, a high-voltage fault occurs, in which the grid voltage increases to 1.35 p.u. within 10 ms. With no protection, the peak value of the rotor current reaches 4.68 p.u.. With the proposed scheme, the peak rotor current is reduced to 1.44 p. u., and the fault-current-limiting rate is 69.2%, as shown in Fig. 7(b).

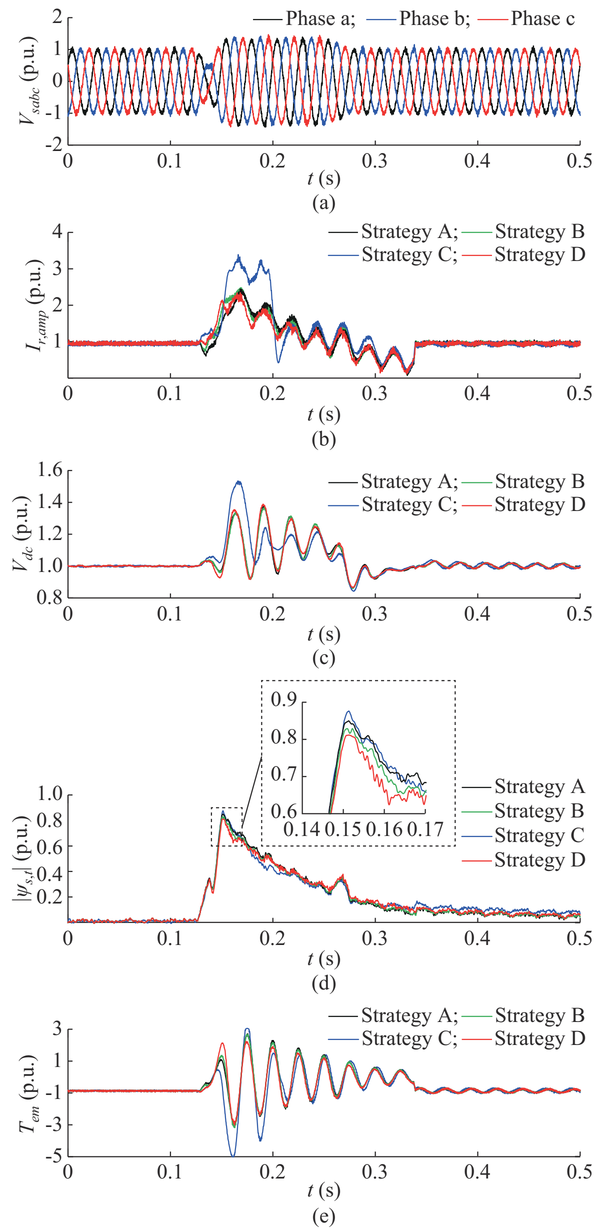

Fig. 6. Simulation results of DFIG with different control strategies under single continuous fault. (a) Stator voltage. (b) Rotor current amplitude. (c) DC-link voltage. (d) Transient flux amplitude. (e) Electromagnetic torque.

Although the peak rotor current of Scheme C is 3.74 p.u., an energy storage converter with the same capacity as the RSC is connected in parallel with the rotor, and the peak output current of the RSC is 1.87 p.u., which is still greater than that of the proposed scheme. The proposed scheme can effectively limit the rotor overcurrent and protect the RSC. In conventional VC, the continuous fault causes excess energy to accumulate on the DC-link capacitor, resulting in an increase in the DC voltage to 1.99 p.u.. In Schemes B and C, the peak values of the DC-link voltage are 1.22 and 1.08 p. u., respectively. However, the lowest value of the DC-link voltage is 0.73 p.u. for Scheme B, which is below the safety threshold of the DC-link voltage. With the help of the DC chopper in proposed scheme, the peak value of the DC voltage is 1.08 p.u., and the DC-link voltage-limiting rate is 45.7%.

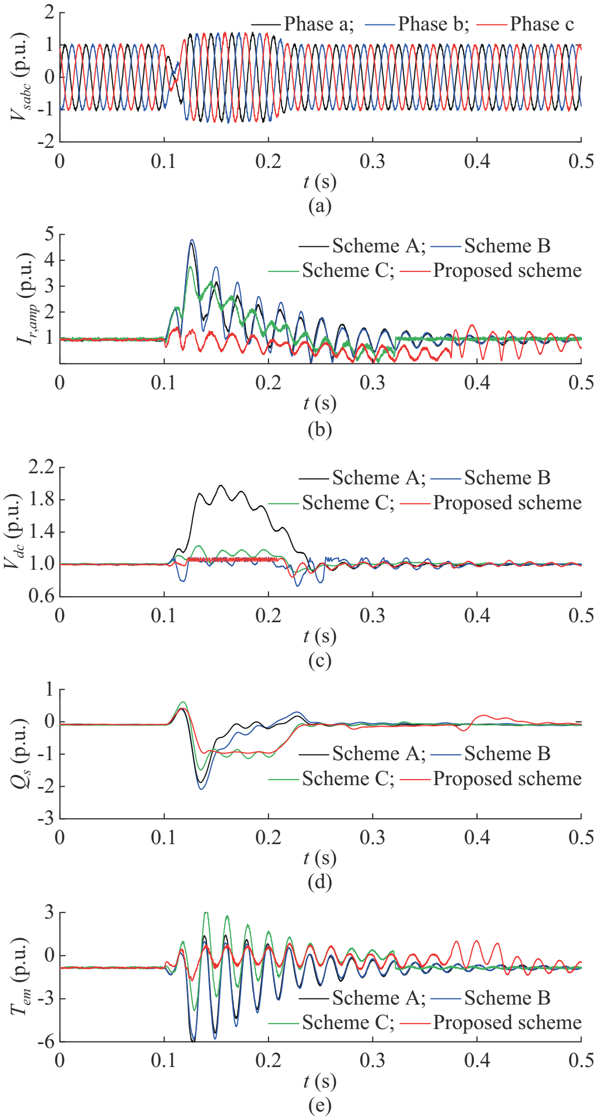

Fig. 7. Simulations results of DFIG under a single continuous fault with different schemes. (a) Stator voltage. (b) Rotor current amplitude. (c) DC-link voltage. (d) Reactive power. (e) Electromagnetic torque.

It can be observed from Fig. 7(d) that the DFIG outputs and absorbs the specified reactive power according to the PCC voltage using reactive power control. When the voltage decreases to 0.1 p.u., the corresponding reactive power of the stator is 0.42 p.u.. When the voltage is maintained at 1.35 p.u., the reactive power of the stator is −0.95 p.u.. As shown in Fig. 7(e), the minimum and maximum electromagnetic torques are −6.04 and 1.43 p.u., respectively. The electromagnetic torque will seriously fluctuate when there is no protection, which will damage the mechanical system of the DFIG. The minimum and maximum electromagnetic torques are only −1.84 and 0.74 p.u., respectively, when adopting the proposed scheme, which significantly suppresses fluctuations of the electromagnetic torque. The limiting rate of torque oscillation is 65.5%.

C. Behaviors Under Multiple Continuous Faults

The occurrence of multiple CFs may result in multiple continuous faults. Simulation results of DFIG under multiple continuous faults with different schemes are shown in Fig. 8. With the proposed scheme, the peak value of the rotor current is reduced from 4.27 p.u. to 1.52 p.u., as shown in Fig. 8(b). The rotor current-limiting rates with Scheme C and the proposed scheme are 11.2% and 64.4%, respectively. When there is no protection, multiple low- and high-voltage continuous faults cause excess energy to accumulate on the DC capacitor, causing the DC voltage to rise to 2.07 p.u.. As in Fig. 8(c), the DC-link voltage-limiting rates in Scheme B, Scheme C, and the proposed scheme are 43.5%, 47.8%, and 47.8%, respectively. According to Fig. 8(d), the DFIG can still generate or absorb reactive power during multiple continuous faults, which is beneficial to the recovery of the grid voltage. When the voltage decreases to the minimum value and increases to the maximum value, the corresponding reactive power of the stator is 0.41 and −0.39 p.u., respectively. As shown in Fig. 8(e), the electromagnetic torque will severely fluctuate when there is no protection during the fault.

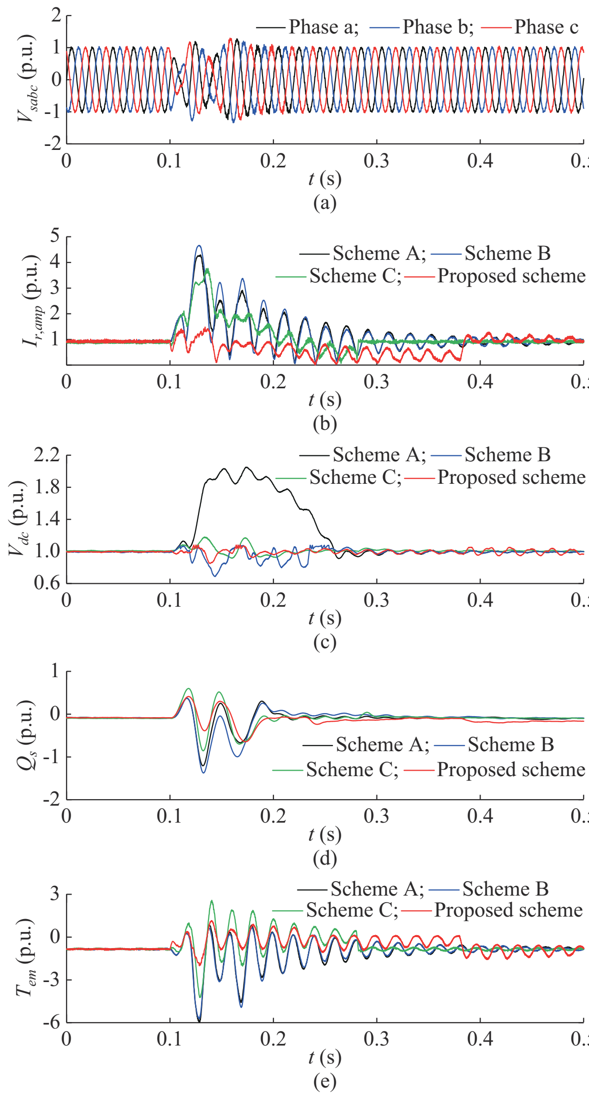

Fig. 8. Simulations results of DFIG under multiple continuous faults with different schemes. (a) Stator voltage. (b) Rotor current amplitude. (c) DC-link voltage. (d) Reactive power. (e) Electromagnetic torque.

The minimum and maximum values are −5.94 p.u. and 0.84 p.u., respectively, and the peak-to-peak value is 6.78 p.u.. With the proposed scheme, the electromagnetic torque is restrained between −1.98 p.u. and 1.14 p.u.. Thus, the rate for limiting torque oscillation is 54.0%. It can be observed that the proposed scheme can still achieve better transient response under multiple continuous faults and help DFIGs successfully ride through continuous faults.

V. Conclusion

This paper proposes an effective scheme to enhance the continuous FRT capability for DFIGs when CFs occur in LCC-HVDC transmission systems. The core idea is to combine a series impedance circuit on the rotor side with coordinated control to protect the RSC and accelerate the attenuation of the transient flux of the stator. The effectiveness of the scheme is verified under different continuous faults. The main conclusions are as follows.

1) Improved demagnetization control without filters is proposed for continuous faults, which can weaken the EMF of the rotor caused by the accumulation effect of the flux.

2) The design and operation principles of the series impedance circuit integrated on the rotor side are provided. Considering a continuous fault, a design method is provided for this circuit.

3) Coordinated control of the demagnetization and reactive currents is proposed. Segmented reactive current control can meet the requirements of grid codes during the low- and high-voltage stages.

References

[1] N. Zhang, H. Jiang, Y. Li *et al*., "Aggregating distributed energy storage: cloud-based flexibility services from China," *IEEE Power and Energy Magazine*, vol. 19, no. 4, pp. 63-73, Jul.-Aug. 2021.

[2] J. Tu, J. Zhang, S. Ma *et al*., "Mechanism analysis and control measures of wind turbine generators tripping caused by HVDC contingencies," in *Proceedings of 12th IET International Conference on AC and DC Power Transmission (ACDC 2016)*, Beijing, China, May 2016, pp. 1-7.

[3] C. Wang and B. Liu, "Affects of commutation failure in multi-circuit HVDC transmission system interconnecting regional power grids on AC power system at sending end," *Power System Technology*, vol. 37, no. 4, pp. 1052-1057, Apr. 2013.

[4] M. Li, "Characteristic analysis and operational control of large-scale hybrid UHV AC/DC power grids," *Power System Technology*, vol. 40, no. 4, pp. 985-991, Apr. 2016.

[5] J. Ren, Y. Wang, Z. Zheng *et al*., "Signature POWIs for DFIG under LVRT conditions: analysis, experiments and recommendations," *International Journal of Electrical Power & Energy Systems*, vol. 136, p. 107622, Mar. 2022.

[6] Z. Zheng, J. Ren, X. Xiao *et al*., "Response mechanism of DFIG to transient voltage disturbance under commutation failure of LCC-HVDC System," *IEEE Transactions on Power Delivery*, vol. 35, no. 6, pp. 2972-2979, Dec. 2020.

[7] T. Zhang, J. Yao, P. Sun *et al*., "Improved continuous fault ride through control strategy of DFIG-based wind turbine during commutation failure in the LCC-HVDC transmission system," *IEEE Transactions on Power Electronics*, vol. 36, no. 1, pp. 459-473, Jan. 2021.

[8] J. Bauman and M. Kazerani, "Commutation failure reduction in HVDC systems using adaptive fuzzy logic controller," *IEEE Transactions on Power Systems*, vol. 22, no. 4, pp. 1995-2002, Nov. 2007.

[9] H. Son and H. Kim, "An algorithm for effective mitigation of commutation failure in high-voltage direct-current systems," *IEEE Transactions on Power Delivery*, vol. 31, no. 4, pp. 1437-1446, Aug. 2016.

[10] J. Wen, J. Wang, L. Wang *et al*., "Evaluation of capacitor commutated converter HVDC for Qinghai-Xizhang interconnection project," in *Proceedings of 9th IET International Conference on AC and DC Power Transmission*, London, UK, Oct. 2010, pp. 1-5.

[11] Q. Wang, T. Li, X. Tang *et al*., "Study on the site selection for synchronous condenser responding to commutation failures of multi-infeed HVDC system," *The Journal of Engineering*, vol. 2019, no. 16, pp. 1413-1418, Jan. 2019.

[12] Y. Zhou, H. Wu, W. Wei *et al*., "Optimal allocation of dynamic var sources for reducing the probability of commutation failure occurrence in the receiving-end systems," *IEEE Transactions on Power Delivery*, vol. 34, no. 1, pp. 324-333, Feb. 2019.

[13] J. Burr, S. Finney, and C. Booth, "Comparison of different technologies for improving commutation failure immunity index for LCC HVDC in weak AC systems," in *Proceedings of 11th IET International Conference on AC and DC Power Transmission*, Birmingham, UK, Feb. 2015, pp. 1-7.

[14] D. Xiang, L. Ran, and P. J. Tavner, "Control of a doubly fed induction generator in a wind turbine during grid fault ride-through," *IEEE Transactions on Energy Conversion*, vol. 21, no. 3, pp. 652-662, Sept. 2006.

[15] R. Zhu, Z. Chen, Y. Tang *et al*., "Dual-loop control strategy for DFIG-based wind turbines under grid voltage disturbances," *IEEE Transactions on Power Electronics*, vol. 31, no. 3, pp. 2239-2253, Mar. 2016.

[16] J. Liang, W. Qiao, and R. Harley, "Feed-forward transient current control for low-voltage ride-through enhancement of DFIG wind turbines," *IEEE Transactions on Energy Conversion*, vol. 25, no. 3, pp. 836-843, Sept. 2010.

[17] Y. Chang, I. Kocar, J. Hu *et al*., "Coordinated control of DFIG converters to comply with reactive current requirements in emerging grid codes," *Journal of Modern Power Systems and Clean Energy*, vol. 10, no. 2, pp. 502-514, Mar. 2022.

[18] A. M. A. Haidar, K. M. Muttaqi, and M. T. Hagh, "A coordinated control approach for DC link and rotor crowbars to improve fault ride-through of DFIG-based wind turbine," *IEEE Transactions on Industry Applications*, vol. 53, no. 4, pp. 4073-4086, Jul.-Aug. 2017.

[19] Y. K. Gounder, D. Nanjundappan, and V. Boominathan, "Enhancement of transient stability of distribution system with SCIG and DFIG based wind farms using STATCOM," *IET Renewable Power Generation*, vol. 10, no. 8, pp. 1171-1180, May 2016.

[20] G. Rashid and M. H. Ali, "Transient stability enhancement of doubly fed induction machine-based wind generator by bridge-type fault current limiter," *IEEE Transactions on Energy Conversion*, vol. 30, no. 3, pp. 939-947, Sept. 2015.

[21] G. Rashid and M. H. Ali, "Nonlinear control-based modified BFCL for LVRT capacity enhancement of DFIG-based wind farm," *IEEE Transactions on Energy Conversion*, vol. 32, no. 1, pp. 284-295, Mar. 2017.

[22] W. Christian, G. Fabian, and W. F. Friedrich, "Fault ride-through of a DFIG wind turbine using a dynamic voltage restorer during symmetrical and asymmetrical grid faults," *IEEE Transactions on Power Electronics*, vol. 26, no. 3, pp. 807-815, Mar. 2011.

[23] Z. Zou, X. Chen, C. Li *et al*., "Conceptual design and evaluation of a resistive-type SFCL for efficient fault ride through in a DFIG," *IEEE Transactions on Applied Superconductivity*, vol. 26, no. 1, p. 5600209, Jan. 2016.

[24] J. Ren, X. Xiao, Z. Zheng *et al*., "A SMES-based dynamic current limiter to improve the LVRT capability of DFIG-based WECS," *IEEE Transactions on Applied Superconductivity*, vol. 31, no. 8, pp. 1-5, Nov. 2021.

[25] X. Xiao, R. Yang, X. Chen *et al*., "Enhancing fault ride-through capability of DFIG with modified SMES-FCL and RSC control," *IET Generation, Transmission & Distribution*, vol. 12, no. 1, pp. 258-266, Jan. 2018.

[26] Z. Xie, X. Zhang, X. Zhang *et al*., "Improved ride-through control of DFIG during grid voltage swell," *IEEE Transactions on Industrial Electronics*, vol. 62, no. 6, pp. 3584-3594, Jun. 2015.

[27] L. Sun and Y. Wang, "Analysis and performance evaluation for transient whole process of improved control strategy for doubly-fed induction generator crossed by high voltage ride through," *High Voltage Engineering*, vol. 45, no. 2, pp. 593-599, Feb. 2019.

[28] C. Zhou, Z. Wang, P. Ju *et al*., "High-voltage ride through strategy for DFIG considering converter blocking of HVDC system," *Journal of Modern Power Systems and Clean Energy*, vol. 8, no. 3, pp. 491-498, May 2020.

[29] P. Song, Y. Zhang, K. Bai *et al*., "High voltage ride-through control method for DFIG-based wind turbines based on resonant controller," in *Proceedings of 2016 IEEE International Conference on Power and Renewable Energy (ICPRE)*, Shanghai, China, Oct. 2016, pp. 67-71.

[30] Z. Zheng, G. Yang, and H. Geng, "High voltage ride-through control strategy of grid-side converter for DFIG-based WECS," in *Proceed-*

ings of 39th Annual Conference of the IEEE Industrial Electronics Society, Vienna, Austria, Nov. 2013, pp. 5282-5287.

[31] J. Li, K. Jiang, G. Liu *et al*., "High voltage ride-through control strategy of doubly-fed induction generator based wind turbines with a series grid-side converter," *Power System Technology*, vol. 38, no. 11, pp. 3037-3044, Nov. 2014.

[32] A. D. Falehi and M. Rafiee, "LVRT/HVRT capability enhancement of DFIG wind turbine using optimal design and control of novel PID-AMLI based DVR," *Sustainable Energy, Grids and Networks*, vol. 16, pp. 111-125, Dec. 2018.

[33] H. Jiang, S. Wang, X. Li *et al*., "Accurate analysis of transient characteristics and ride-through scheme under DFIG low and high voltage cascading fault," *Power System Technology*, vol. 45, no. 10, pp. 4076-4083, Feb. 2021.

[34] L. Hong, X. Zhou, Y. Liu *et al*., "Analysis and improvement of the multiple controller interaction in LCC-HVDC for mitigating repetitive commutation failure," *IEEE Transactions on Power Delivery*, vol. 36, no. 4, pp. 1982-1991, Aug. 2021.

[35] L. Liu, S. Lin, J. Liu *et al*., "Analysis and prevention of subsequent commutation failures caused by improper inverter control interactions in HVDC systems," *IEEE Transactions on Power Delivery*, vol. 35, no. 6, pp. 2841-2852, Dec. 2020.

[36] D. Zhu, X. Zou, L. Deng *et al*., "Inductance-emulating control for DFIG-based wind turbine to ride-through grid faults," *IEEE Transactions on Power Electronics*, vol. 32, no. 11, pp. 8514-8525, Nov. 2017.

[37] Y. Ling, X. Cai, and N. Wang, "Rotor current transient analysis of DFIG-based wind turbines during symmetrical voltage faults," *Energy Conversion and Management*, vol. 76, pp. 910-917, Dec. 2013.

[38] L. Zhou, J. Liu, and S. Zhou, "Improved demagnetization control of a doubly-fed induction generator under balanced grid fault," *IEEE Transactions on Power Electronics*, vol. 30, no. 12, pp. 6695-6705, Dec. 2015.

[39] Y. Shen, D. Ke, Y. Sun *et al*., "Advanced auxiliary control of an energy storage device for transient voltage support of a doubly fed induction generator," *IEEE Transactions on Sustainable Energy*, vol. 7, no. 1, pp. 63-76, Jan. 2016.

Zixuan Zheng received the B.S. and Ph.D. degrees in electrical engineering from Sichuan University, Chengdu, China, in 2012 and 2017, respectively. He is currently an Associate Professor with the College of Electrical Engineering, Sichuan University. His research interests include power quality and operation and control of distributed energy resources.

Donghui Song received the B.Eng. degree in electrical engineering and its automation from Sichuan University, Chengdu, China, in 2021, where he is currently working toward the M.Sc. degree in electrical engineering. His research interests include power quality and renewable energy.

Kaijian Du received the B.Eng. degree in electrical engineering and its automation from Sichuan University, Chengdu, China, in 2016, where he is currently working toward the Ph.D. degree in electrical engineering. His research interests include power electronic converters and wind energy generation systems.

Xianyong Xiao received the B.S., M.S., and Ph.D. degrees in electrical engineering from Sichuan University, Chengdu, China, in 1990, 1998, and 2010, respectively. He is currently a Professor with the College of Electrical Engineering, Sichuan University. His research interests include power quality, smart distribution system, power system catastrophic event, uncertainty theory, and uncertain measures applied to power systems.

Jie Ren received the B.Eng. degree in electrical engineering and its automation from Sichuan University, Chengdu, China, in 2017, where she is currently working toward the Ph.D. degree in power system and its automation. Her research interests include renewable energy generation and fault ride through of wind turbine generators.

Qi Xie received the B.Eng. degree in electrical engineering and its automation from Sichuan University, Chengdu, China, in 2019, where he is currently working toward the M.Sc. degree in electrical engineering. His research interests include power quality and renewable energy.